



Construction atomic-level N-P charge transfer channel for boosted CO₂ photoreduction

Zheyang Liu^{a,1}, Jianli Liang^{b,1}, Qianqian Song^c, Yang Li^b, Zhiquan Zhang^a, Min Zhou^a, Wei Wei^a, Hui Xu^{a,*}, Chun-Sing Lee^b, Huaming Li^a, Zhifeng Jiang^{a,*}

^a Institute for Energy Research, Jiangsu University, Zhenjiang 212013, PR China

^b Department of Chemistry & Center of Super-Diamond and Advanced Films (COSDAF), City University of Hong Kong, 83 Tat Chee Avenue, Kowloon 999077, Hong Kong, China

^c Department of Materials Science and Engineering, Sun Yat-Sen University, Guangzhou, Guangdong 510275, PR China

ARTICLE INFO

Keywords:

Carbon nitride nanotube
Black phosphorus quantum dots
CO₂ photoreduction

ABSTRACT

Efficient conversion of CO₂ to high value-added chemical products is a promising strategy for achieving carbon neutrality. Although the photocatalyst technique has been made widespread researched, highly efficient photoreduction CO₂ with metal-free photocatalysts remains a challenge. Herein, we report a zero-dimensional black phosphorus quantum dots (BPQDs)-decorated one-dimensional carbon nitride nanotubes (CNNT) photocatalyst that reduces CO₂ to CO with a rate of 44.6 μmol g⁻¹ h⁻¹, which is better than the similar photocatalysts and pristine carbon nitride nanotubes. Synchrotron radiation XAFS measurements substantiate the construction of N-P electron transfer channels within BPQDs and CNNT. Time-resolved PL spectrum demonstrates the faster separated electron hole pairs. In situ irradiated X-ray photoelectron spectroscopy confirms the photogenerated-electron flow trend and the active site of photocatalytic reaction. Moreover, the main intermediate *COOH is verified by in situ FT-IR characterization which is corresponding to the previous research. The construction of atomic-level N-P charge transfer channel efficiently facilitates the charge transfer and accelerates the catalytic rate. This work provides a novel insight into the design of BPQDs-anchoring heterostructures for photocatalytic CO₂ reduction.

1. Introduction

Among the multitudinous greenhouse gas, carbon dioxide (CO₂) has risen from 280 ppm to 419 ppm after the industrial revolution, accompanied by the infinite energy demand resulting from civilization development and scientific process supplied by fossil fuels [1–4]. Carbon balance and Zero-CO₂ emission are important for slowing down global warming and other relevant environmental issues [5]. There are two approaches to realizing carbon neutrality: exploit renewable clean energy to reduce fossil fuel burning and strike a balance between carbon emissions and CO₂ utilization [6,7]. Photocatalytic CO₂ reduction reaction (CO₂RR) has attracted substantial attention, since the conversion of CO₂ into high value-added products is an entrancing strategy to kill two birds with one stone of disposing of CO₂ emission problem and obtain profitable fuel [8,9].

Previous researches suggest that g-C₃N₄ is a promising metal-free

photocatalyst on account of its simple synthesis method, visible-light activity, and characteristic layer structure [10–12]. However, bulk g-C₃N₄ exhibits unsatisfactory photocatalytic activity due to the low separation efficiency of photogenerated charge carriers and meager catalytic sites. In general, the regular one-dimensional nanostructure is fascinating in the field of photocatalysis, which shows abundant exposed active sites and superior charge transport [13]. Therefore, the design and preparation of one-dimensional g-C₃N₄ shall be expected to improve its photocatalytic efficiency. Moreover, cocatalysts loading has been demonstrated to be an effective strategy to promote separation of electron-hole pairs and lower reaction level barriers. For example, Shi and co-workers anchored Pt on defective carbon nitride for highly selective photocatalytic CO₂ methanation with water vapor [9]. Li's group decorated copper single atoms to crystalline carbon nitride for nearly 100% CO selectivity [14]. Chen and coworkers fabricated La single-atoms on carbon nitride with La-N charge-transfer bridge for

* Corresponding authors.

E-mail addresses: xh@ujs.edu.cn (H. Xu), jiangzf@ujs.edu.cn (Z. Jiang).

¹ These authors contributed equally to this work.

highly efficient and selective photoreduction of CO_2 to CO [15]. Whereas, these metal-based even noble metal-based co-catalysts seriously hinder the development of CO_2 photoreduction since the limitation of high price and sparse yield [16,17]. Hence, it is believed that exploit and prepare a high-efficient, innocuous and readily available co-catalyst are imminent.

Recently, 2D BP have been widely reported for catalytic reaction [18,19]. Whereas, in consideration of the more remarkable extinction ability and catalytic sites than the 2D and bulk phase, 0D BPQDs are supposed to be more ideal photocatalytic semiconductor [20,21]. Notably, inspired by the quantum confinement effect and edge state effect, BPQDs present the distinct electronic and optical characteristics which suggests the potential application of BPQDs in the field of photocatalysis [22–24]. In previous works, BP hybrids were widespread applied in pollutant degradation and hydrogen evolution, ignoring the development prospect of BP hybrids in the field of CO_2 RR [25,26]. Therefore, coupling BPQDs with CNNT to fabricate a metal-free photocatalyst for CO_2 photoconversion may be a promising strategy to realize carbon-neutral.

In this work, ultrasmall BPQDs were uniformly decorated on the surface of CNNT via electrostatic self-assembly strategy to construct 0D–1D nanoscale hybrid catalyst, which remarkably improved the activity for the photoreduction of CO_2 to CO. The surface anchoring of BPQDs could form a strong P–N bond with CNNT, verified by XANES spectroscopy and DFT, which highly enhanced the photogenerated charge carriers transfer and separation efficiency. Furthermore, in situ XPS was performed to confirm the photogenerated electron transport path and determine the stable N sites in the C–N heterocyclic ring are the destination of electron flow [27,28]. In consideration of the effect of BPQDs for electron orientation induction, the CO evolution rates were distinctly promoted by nearly 3 times from 9.3 to $27.7 \mu\text{mol}\cdot\text{g}^{-1}\cdot\text{h}^{-1}$ and it can be raised to $44.6 \mu\text{mol}\cdot\text{g}^{-1}\cdot\text{h}^{-1}$ under the certain condition.

2. Experimental section

2.1. Materials

Red phosphorus, tin, and iodine were purchased from Alfa Aesar Technology Co., Ltd. hydroxylamine hydrochloride ($\text{HONH}_2\cdot\text{HCl}$), and melamine ($\text{C}_3\text{N}_6\text{H}_6$) were purchased from Aladdin Biochemical Technology Co., Ltd. All chemicals were of analytical reagent grade and used without further purification.

2.2. Preparation of g- C_3N_4 nanotubes (CNNT)

The g- C_3N_4 nanotube was synthesized based on a two-step method. In detail, 4 g hydroxylammonium chloride and 2 g melamine were first added into 70 mL deionized water with ultrasonic and stirring for a total of 2 h. The mixture solution was transferred into a Teflon lined autoclave at 120°C for 12 h. The obtained intermediates were washed three times with deionized water and freeze-drying. Ultimately, the intermediate was added to porcelain boat and heated at 520°C under Air atmospheres for 4 h with a heating rate of $2^\circ\text{C}/\text{min}$.

2.3. Preparation of bulk BP

Bulk BP was synthesized via a typical phase transformation method our group reported before. 30 mg of tin powder, 25 mg of iodine, and 350 mg of red phosphorus are put in a silica glass ampoule (100 mm length, an inner diameter of 8 mm and a wall thickness of 1 mm). The mixture was heated from room temperature to 600°C with a heating rate of $5^\circ\text{C}/\text{min}$, and kept for 5–10 h at 600°C . Finally, sub-4 mm-sized bulk BP single crystals were obtained.

2.4. Preparation of BPQDs

In brief, BPQDs were synthesized by a typical liquid exfoliation method. 30 mg of bulk BP powders were dispersed into 30 mL of deionized water, and then vacuum and bubble with argon to further remove the dissolved oxygen. The suspension was sonicated with a sonic tip for 6 h at the power of 600 W. The ultrasound probe worked for 2 s with an interval of 4 s. Then the dispersion was sonicated in an ultrasonic bath for 12 h at the power of 360 W at 0°C . After that, the solution was centrifuged at 7000 rpm for 20 mins and the supernatant containing BPQDs was collected. The obtained solution was stored in a low temperature and dark environment for further employment.

2.5. Preparation of black phosphorus quantum dots/carbon nitride nanotubes hybrids (BPQDs/CNNT)

BPQDs/CNNT hybrids were synthesized by a facile electrostatic-driven self-assembling approach. In brief, 20 mg CNNT was first added into 20 mL deionized water and then transferred into a closed glass container. A certain amount of BPQDs suspension was added to the CNNT solution. After bubbling with argon for 10 mins the dispersion was sonicated for 1 h and stirred for 12 h. The prepared hybrids were CNNT loading 1.0 wt%, 2.0 wt%, 3.0 wt%, and 4.0 wt% BPQDs.

2.6. Photocatalytic CO_2 reduction

The photocatalytic CO_2 reduction performance for each sample was evaluated at a low temperature (10°C) using a 300 W Xe lamp (PLS-SXE 300 C (BF), Beijing Perfectlight) as the light source. The reaction was performed in a 250 mL offline photocatalytic reactor equipped with a quartz window on the top. 10 mg of the photocatalyst was fully dispersed in 12 mL H_2O solution, and 4 mL of sacrificial electron donor triethanolamine (TEOA) was added. Then, pump air inside the container and fill pure CO_2 (99.999%) three times to make sure the gas in the container is CO_2 . Finally, keep the pressure inside the reactor at nearly 100 kPa. The generated gas products were analyzed by gas chromatograph (GC9790II(PLF-01), Fuli, Zhejiang).

3. Results and discussion

3.1. Characterization of as-prepared materials

As shown in Fig. S1, the Raman spectrum of the fabricated material verified that the used material is black phosphorus. As shown in Fig. 1a, ultrasmall BP quantum dots suspension was obtained by secondary ultrasonic stripping on the basis of bulk BP. Meanwhile, $\text{C}_3\text{H}_6\text{N}_6$ and $\text{HONH}_2\cdot\text{HCl}$ (the mass ratio is 1:2) were transferred to the Teflon lined autoclave, hydrothermal at 120°C for 12 h to gain CN nanorods precursor and then calcined it in Air to obtain CNNT. Ultimately, the BPQDs/CNNT 0D/1D hybrid structure was fabricated via a simple electrostatic self-assembly approach. Zeta potential measurements (Fig. 1b) show that the surface charge of the CNNT and BPQDs is on the contrary in deionized water, with the zeta potential values measured as $+5$ mV and -37.6 mV, respectively. CNNT could be protonated easily in an aqueous solution $\text{PH} < 7$, further promoting the CNNT surface being positively charged [29]. Therefore, what can be expected is the emergence of spontaneous self-assembly between the negatively charged BPQDs and the positively charged CNNT through electrostatic interaction for the construction of the BPQDs/CNNT 0D/1D hybrid structure.

The morphologies of CNNT, BPQDs, and BPQDs/CNNT were characterized by Scanning electron microscope (SEM) and transmission electron microscopy (TEM), respectively. As shown in Fig. 1c and 1d, the average diameter of the pristine CNNT is about 100–200 nm, and CNNT exhibits a relatively regular 1D tubular structure, proving that the morphology of C_3N_4 was successfully modified. X-ray diffraction (XRD)

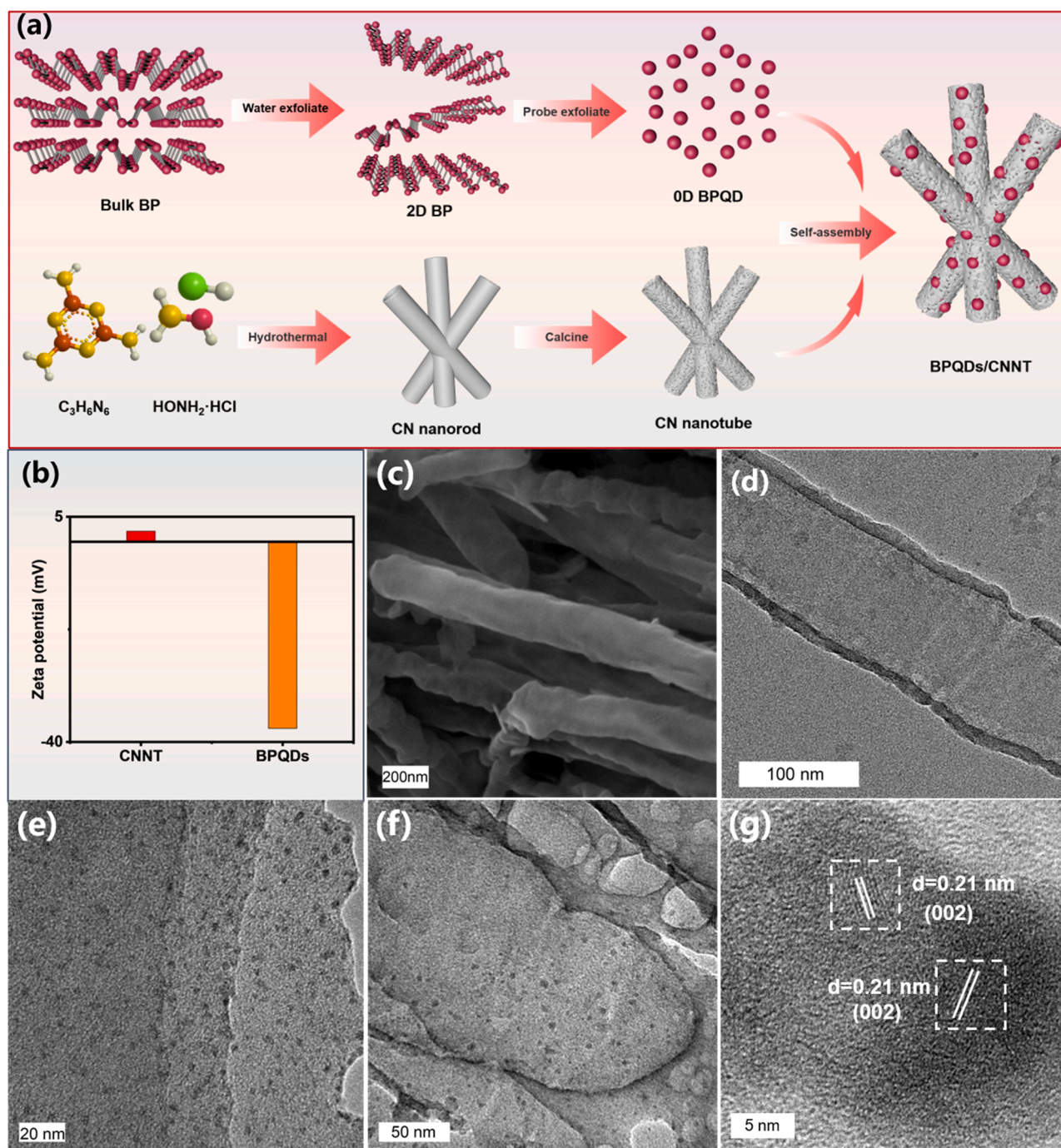


Fig. 1. (a) Synthetic route of BPQDs@CNNT. (b) Zeta potential of the CNNT and BPQDs dispersed in deionized water at pH 7. SEM images of (c) CNNT. TEM images of (d) CNNT, (e) BPQDs, and (f) BPQDs/CNNT hybrid. (g) HRTEM image of BPQDs/CNNT.

analysis further verifies the formation of in-based $g-C_3N_4$ (Fig. S2) [30]. The BPQDs show homogeneous dot structure with an average diameter of 3–5 nm (Fig. 1e). As shown in Fig. 1f, a mass of black spots is uniformly distributed on the surface of CNNT, implying that the BPQDs and CNNT are probably composited successfully. In the meanwhile, there is almost no difference in XRD patterns of CNNT and BPQDs/CNNT (Fig. S1), indicating that the very small amount of BPQDs on the surface of CNNT, and the physical structure of CNNT was still consistent with the initial phase after deposition of BPQDs [31]. The enlarged TEM image (Fig. 1g) shows that the lattice distance of black spots is about 0.21 nm, which is consistent with the (002) crystal plane of BP, further confirming the black spots are BPQDs. The resultant specific surface

areas (S_{BET}) displayed in Fig. S3, with the loading of BPQDs, there is an inconspicuous decrease of S_{BET} from 47.1 m^2/g (original CNNT) to 39.5 m^2/g (BPQDs/CNNT hybrid), which was resulted from the aggregation of QDs in the CNNT mesopores. Fig. S4 shows the Fourier-transform infrared spectra (FTIR) of CNNT and BPQDs/CNNT samples. The spectra of BPQDs/CNNT are parallel to CNNT, the abroad peak centered around 3000 cm^{-1} to 3500 cm^{-1} belong to the stretching modes of N-H and O-H originating from the uncondensed -NH&-NH₂ groups and unadsorbed H₂O molecules on the surface of the catalysts, while the fingerprint peaks situating from 1200 cm^{-1} to 1600 cm^{-1} contributing to the stretching modes of aromatic C-N heterocycles [32, 33]. In addition, the main peak located at 810 cm^{-1} is assigned to the

out-of-plane bending mode of heptazine rings [33]. Interestingly, the IR signals concerned with BPQDs were undetected, and no significantly increasing or decreasing observed in the density of CNNT characteristic peaks, indicating that the addition of BPQDs exerts no influence on the main chemical structure of CNNT [24,34].

X-ray photoelectron spectroscopy (XPS) was carried out to further explore the chemical states of samples. Three typical peaks are decomposed by the C 1s XPS spectrum of the BPQDs/CNNT, which is located at 288.2 eV, 286.6 eV, and 284.8 eV match with the binding energies of N-C=N, C-NHx, and C-C/C=C, respectively [33]. The high-resolution XPS spectra of the N 1s core level is shown in Fig. 2e. The peaks located at 398.6 eV, 400.6 eV and 404 eV can be attributed to the C-N = C, N-(C)3 and, C-NHx bonds, respectively, corresponding to the tri-triazine structure. The high-resolution XPS spectra of the P 2p core-levels (Fig. 2c) display a 2p3/2 and 2p1/2 doublet located at 129.8 and 130.6 eV, respectively [35]. Whereas, compared with the pristine CNNT and BP, there is no significant change detected on the surface chemical state of BPQDs/CNNT, which may be contributed to the trace amounts of ultra-small BPQDs [32,36]. Hence, to demonstrate the accurate chemical environment and the formation of a connection between BPQDs and CNNT, X-ray absorption near-edge structure (XANES) spectroscopy was performed. In Fig. 3d, peak 1 in the π^* regime of the C K-edge spectra is

down-shifted by ~ 0.4 eV towards a lower energy level for BPQDs/CNNT hybrids, which is originating from C-N = C, the broad peak 2 corresponding to σ^* (C-C) shows the similar trend compared with the pristine CNNT [37,38]. Likewise, peak 1 for the N K-edge XANES spectra is ascribed to the excitation of the N 1s core-level electrons to π^* (C=N-C) state, which is shifted by ~ 0.22 eV to a lower energy level. Whereas, compared to pure CNNT, peaks 2, 3 for the N K-edge XANES spectra display similar trends upon decoration with BPQDs, which are assigned to the excitation of the N 1s core-level electrons to π^* (N-(C)3) and σ^* (C-N) states, respectively [38,39]. We further collected P L-edge XANES spectra of the BPQDs/CNNT hybrid and BP. As shown in Fig. 2f, the peak 1 (138.8 eV) at low energy side for the P L-edge XANES spectra corresponding to the transitions from spin-orbit split 2p electrons into the first unoccupied 3s-like antibonding state, which referred to as the L_{2,3}-edge. The broad peak (147 eV) at higher energy contributing to 2p to 3d transitions in elemental P [40, 41]. Interestingly, in the P L-edge XANES spectra of the BPQDs/CNNT hybrid, a new peak 3 has emerged, which is attributed to the transitions to 3p levels in relation to the N containing group, confirming that the formation of N-P bonds. Whereas, the intense signal 4 (144.5 eV) mainly ascribed to the bond with N/C in CNNT [42,43]. Notably, the appearance of the new peak 3 further verifies that there is a strong force

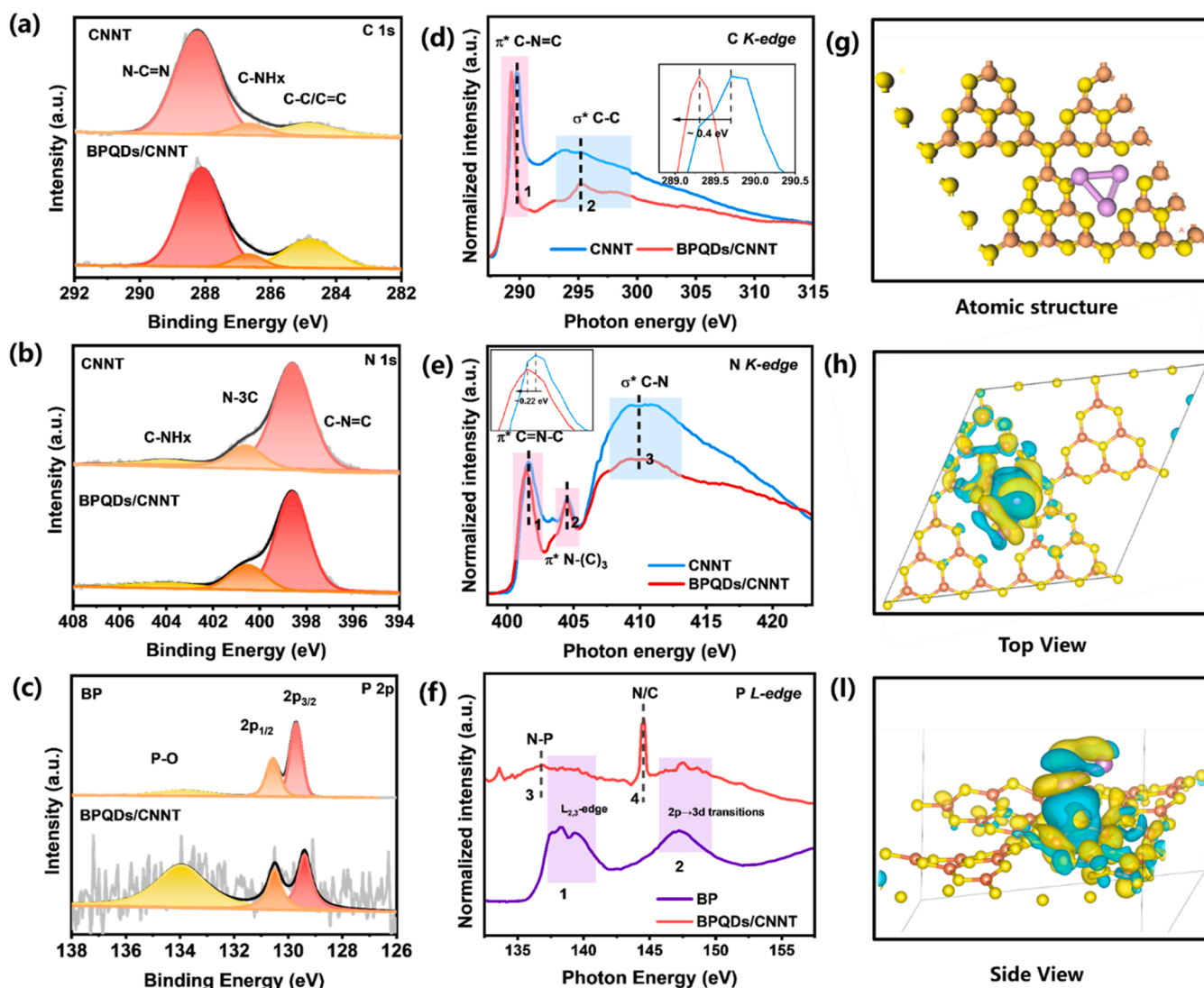


Fig. 2. The high-resolution XPS spectrum of BNNF and BPQDs/CNNT: (a) C 1s, (b) N 1s, and (c) P 2p. Synchrotron radiation XAFS measurements. (d) C K-edge XANES spectra, (e) N K-edge XANES spectra, (f) P L-edge XANES spectra. (g) Atomic structure of BPQDs/CNNT hybrid. (h) Top view and (i) side view of charge carrier intensity distribution of BPQDs/CNNT.

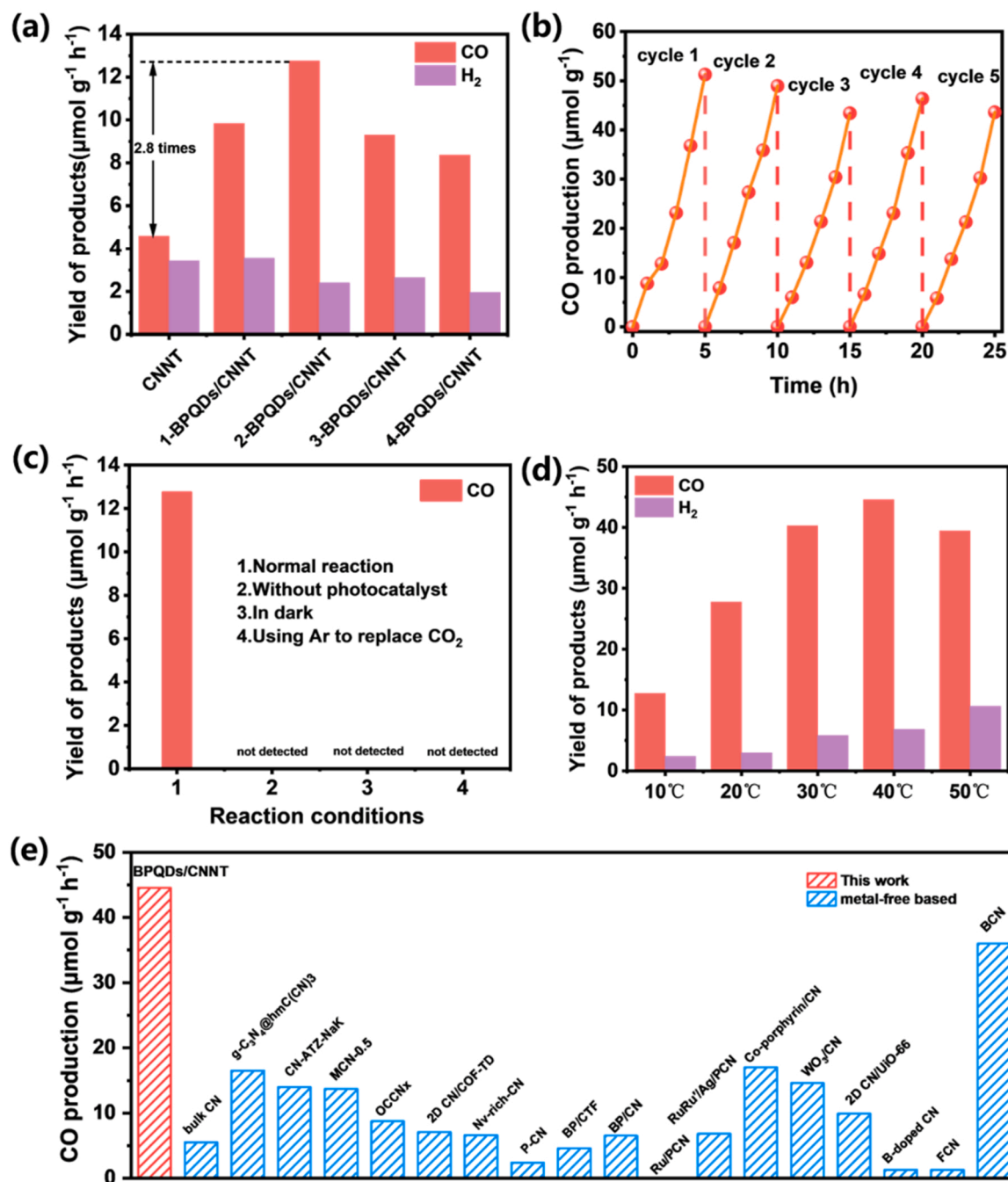


Fig. 3. Photocatalytic CO₂ reduction experiments. (a) the yield of products of the CNNT and BPQDs/CNNT hybrids with the different load amounts of BPQDs at low temperature, (b) recycling test of BPQDs/CNNT for CO₂ photoreduction, (c) CO production over different reaction conditions under UV–visible-light irradiation for 5 h. (d) the yield of products of the BPQDs/CNNT hybrids under different temperatures. (e) summary of some reported metal-free and metal-free based photocatalysts for CO₂RR.

between BPQDs and CNNT rather than a simple physical mixture of two monomers [40,44]. Theoretical calculations also confirm the strong interaction between the BPQDs and CNNT (Fig. 2g-i).

3.2. CO₂ photoreduction activity

The performance of the constructed hybrid BPQDs/CNNT samples in the photocatalytic reduction of CO₂ was tested in a catalytic system driven by UV–vis light and containing TEOA as the electron donor. The yield of products revealed that 2-BPQDs/CNNT hybrid photocatalyst achieves a respectable rate of 12.75 $\mu\text{mol g}^{-1} \text{h}^{-1}$, which was more than the original CNNT by approximately three times. The increase in activity

mainly depends on the excitation of hot electrons and the faster separation of charge carriers by BPQDs decorated. However, loading more BPQDs actually degrades performance, probably contributing to the heavy load of BPQDs resulted in the aggravation of agglomeration and influenced the light absorption of catalysts. Furthermore, the CO selectivity of BPQDs/CNNT also significantly enhanced from 57.2% (CNNT) to 84.2%. More detailed product yields have been shown in Table S1. In addition, the apparent quantum yield of BPQDs/CNNT is about 0.028%. Meanwhile, the parallel photocatalytic CO₂ reduction experiment was tested at room temperature and similar volcanic properties were obtained, further demonstrating that the most suitable load was 2-BPQDs. (Fig.S5) In addition, the 2-BPQDs/CNNT was very stable,

exhibiting a CO production rate that was still up to 85% after five cycles under the same experimental conditions. Furthermore, in consideration of the practical application, photocatalytic CO₂ reduction activity experiments were performed at different temperatures and the CO yield achieved the highest at 313 K, about 44.56 $\mu\text{mol}\cdot\text{g}^{-1}\cdot\text{h}^{-1}$ (Fig. 3d). The CO yield rate is higher than the most of metal-free catalysts and nonmetal-based composite catalysts. (Fig. 3e) Furthermore, the experiment using isotope-labeled ¹³CO₂ was conducted, and the products were measured by GC–MS. The signals located at 29 and 45 are assigned to ¹³CO₂ and ¹³CO, respectively. In addition, it is noted that no signal detected at 28, which verify that the CO product is originated from CO₂. (Fig. S6) In addition, control photocatalytic experiments were conducted to confirm the origin of catalytic products. As shown in Fig. 3c, CO was undetected under the controlled conditions (absence of photocatalysts, using Ar to replace CO₂ or in dark, respectively), confirming that the product CO was converted from the CO₂ rather than the decomposition of the photocatalyst itself and any other carbon contaminants, which is consistent of the results of the ¹³CO₂ isotope experiment. [45].

3.3. Band structure analysis

To explore the mechanism of the enhanced photocatalytic activity, three primary processes were taken into consideration, which contain light absorption, electron-hole pairs separation and surface reactions. As indicated by UV–vis diffuse reflectance spectra, the hybrid catalyst shows the enhanced ability to absorb light compared with the pristine

CNNT, which could be contributed to the full spectrum light absorption capacity of loaded BPQDs. (Fig. 4c) Moreover, to clarify the effect of the band structure changes, ultraviolet photoelectron spectrometer (UPS) was performed to obtain the valance band (VB) of samples and the conduction band (CB) can be calculated based on the bandgap and VB. As displayed in Figs. 4a and 4b, BPQDs/CNNT hybrid (2.65 eV) did not show a significant difference in the bandgap compared to pure CNNT (2.75 eV) and both samples possessed appropriate band structures for the reduction of CO₂ to CO. However, it is noted that although the CB of BPQDs/CNNT located at -0.67 V (vs. RHE) relatively is lower than pure CNNT (-1.05 V), it still substantially satisfied the thermodynamic requirements for converting CO₂ to CO (-0.53 V) [46].

3.4. Electron transport mechanism of photocatalysis

The BPQDs/CNNT photocatalyst facilitates the separation and transfer of photogenerated charge carriers, which can be confirmed by photoluminescence (PL) and photoelectrochemical measurements. Under the same excitation, the reduced PL intensity of photocatalysts suggests the decreased recombination of photogenerated electron-hole pairs after introducing BPQDs (Fig. 5c) [47,48]. Furthermore, time-resolved PL was performed to study the electron migration dynamics on the basis of multi-exponential kinetics. The biexponential fitting results are $(0.295 \pm 0.013)\text{ ns}$ (τ_1), $(1.183 \pm 0.033)\text{ ns}$ (τ_2) and $(4.619 \pm 0.094)\text{ ns}$ (τ_3) for CNNT, while $(0.005 \pm 0.002)\text{ ns}$ (τ_1), $(0.862 \pm 0.020)\text{ ns}$ (τ_2) and $(3.748 \pm 0.101)\text{ ns}$ (τ_3) for BPQDs/CNNT. (Fig. 5d) The calculation of the average emission lifetime $\langle \tau \rangle$ for

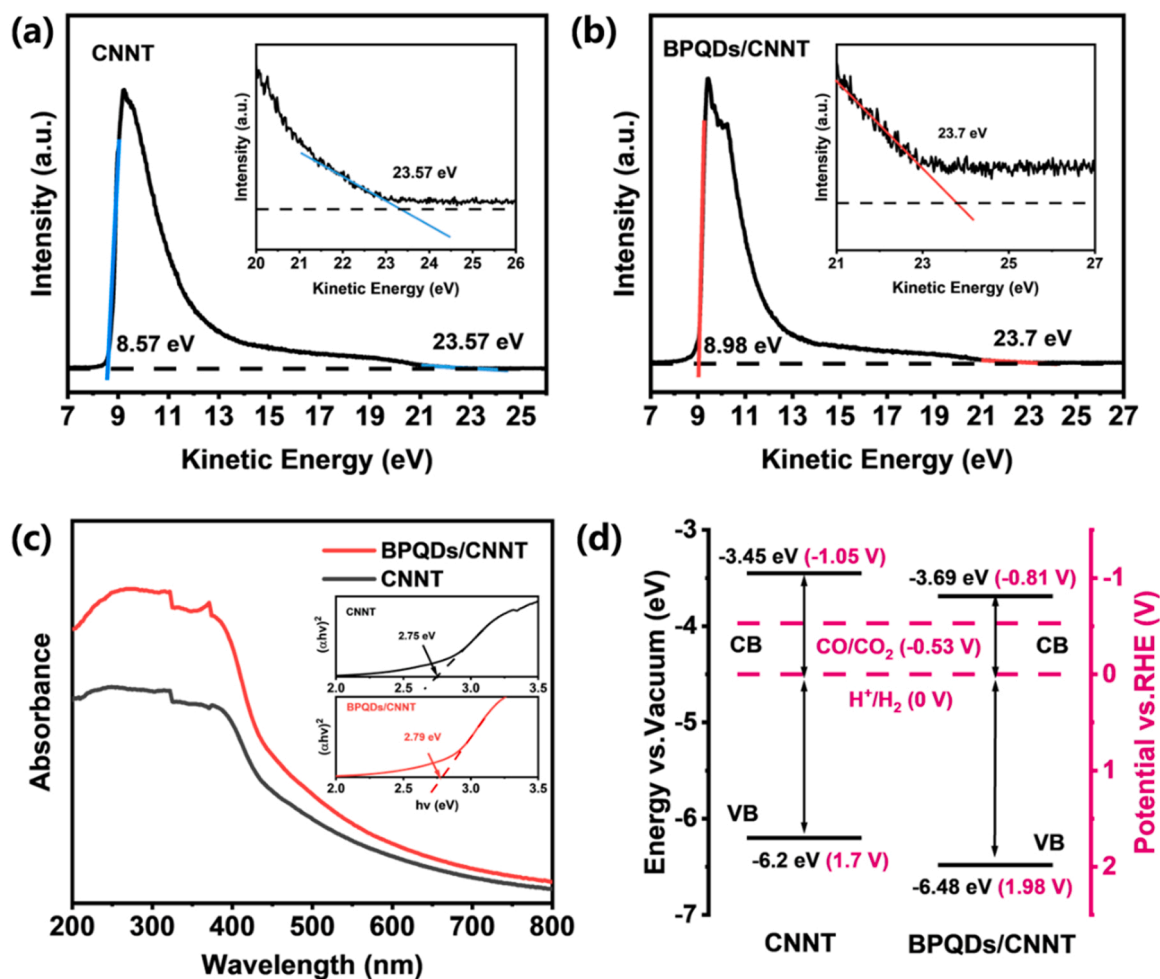


Fig. 4. Ultraviolet photoelectron spectrometer (UPS) of (a) CNNT and (b) BPQDs/CNNT. (c) UV–vis absorption spectrum and Tauc bandgap spectrum. (d) Energy band structure of CNNT and BPQDs/CNNT.

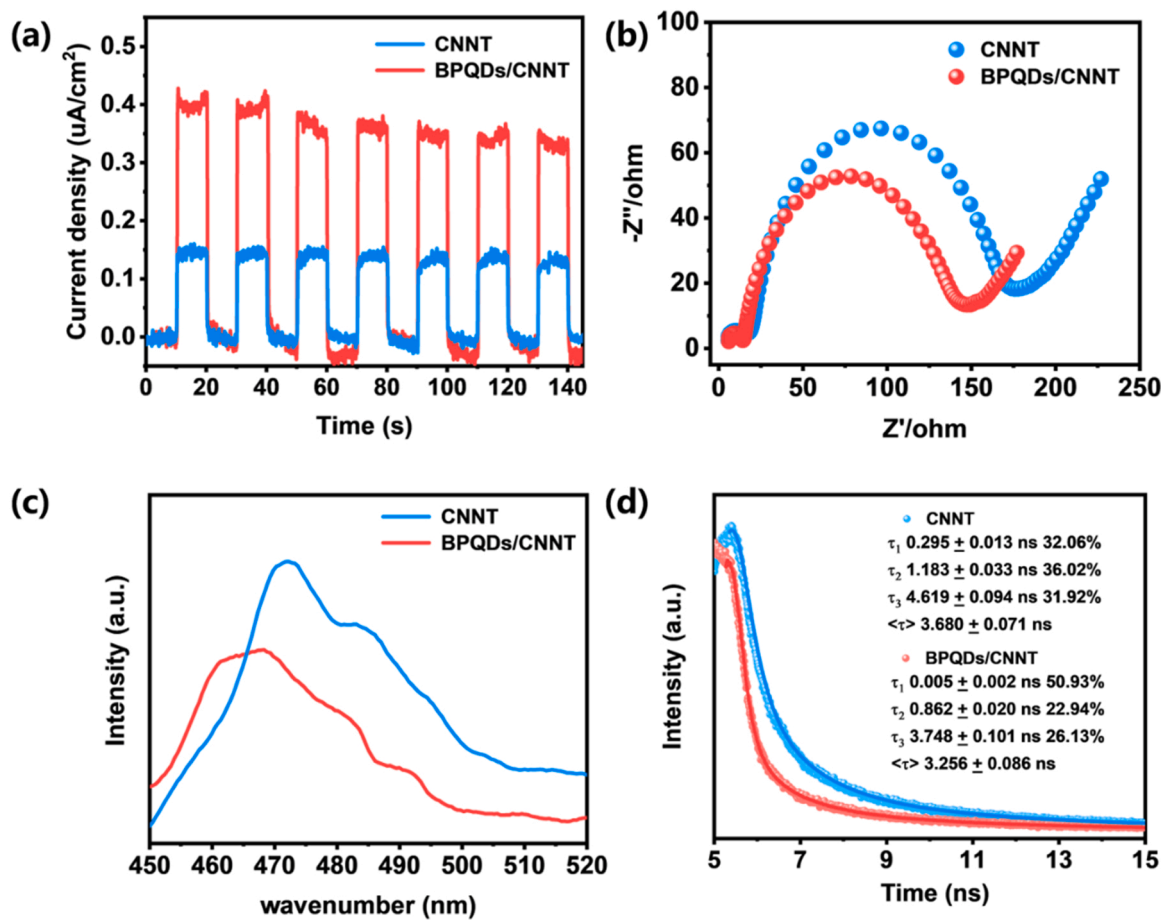


Fig. 5. (a) Photocurrent response under irradiation. (b) Electrochemical impedance spectra of CNNT and BPQDs/CNNT. (c) The room-temperature steady-state PL spectra and (d) time-resolved transient PL decay spectra of CNNT and BPQDs/CNNT hybrids.

CNNT and BPQDs/CNNT hybrids were (3.680 ± 0.071) ns and (3.256 ± 0.086) ns, respectively. In brief, the decreased electron lifetime in BPQDs/CNNT hybrids implied that the interfacial charge transfer represented a nonradiative pathway. Furthermore, the enhanced separated efficiency of the photoinduced charge carriers, [31,49] which can be contributed to the edge-state effect and quantum confinement effect of BPQDs and the construction of electron transfer channels between BPQDs and CNNT [35,50]. The higher photocurrent intensity of BPQDs/CNNT demonstrates the higher photo-response efficiency and the lower resistance value proves the better conductivity (Fig. 5a, 5b) [51]. The above measurements demonstrate that the rational fabrication of BPQDs/CNNT hybrid photocatalyst not only improves the light absorption properties but also facilitates the separation and transfer of photoinduced charge carriers, which supply more opportunities for CO₂ photoreduction.

3.5. Mechanism of the photocatalytic CO₂ reduction

In-situ high-resolution X-ray photoelectron spectroscopy (XPS) was performed to speculate on the changes in surface electronic chemical states and active sites of BPQDs/CNNT hybrids (Fig. 6a-c). After turning off the light, the position of the peak C-N for the C 1 s core level, the peak N-3 C for the N 1 s core level and peak P-O for the P 2p core level return to the original position. The change of binding energy results from the photogenerated electrons transfer under irradiation. Besides, the reduction and increase of binding energy can be assigned to obtain and lose electrons, respectively [27,28]. Accordingly, the photogenerated electrons in hybrid catalysts flow from BP to CN depending on the electron transmission channels of atomic-level N-P during

photocatalysts. Meanwhile, the decreased N-3 C peak for the N 1 s core level further demonstrates that the active N sites are extremely significant in terms of transmitting and utilizing photogenerated charge carriers for CO₂ reduction.

To gain the detailed data on the conversion pathway of photocatalytic CO₂ reduction, in situ Fourier-transform infrared spectroscopy (FT-IR) measurements were implemented for tracking the evolution of reactive intermediates. As exhibited in Fig. S7, it is noted that the peak derived from 1646 cm⁻¹ belongs to O-H vibration in dark. Subsequently, IR peaks manifested on the BPQDs/CNNT photocatalyst under the demands of the simulated photocatalytic CO₂ reaction environment. Notably, there was an inconspicuous peak offset from the O-H peak by 1623 cm⁻¹, which is contributed to HCO₃⁻ group. Besides, as exhibited in Fig. 6d, the new peak at 1296 cm⁻¹ was observed and the peak intensity distinctly increased with constant irradiation, which can be assigned to the vibration of CO₃²⁻ [52]. The peak at 1397 cm⁻¹ and 1456 cm⁻¹ can be ascribed to the asymmetric OCO stretches of the bidentate carbonate (b-CO₃²⁻) group and monodentate carbonate (m-CO₃²⁻) group, respectively [53]. In the meanwhile, the new signals centered around 1210 cm⁻¹ and 1360 cm⁻¹ corresponding to the HCO₃⁻ group and *COOH group, respectively, further indicating that the *COOH group is a key intermediate product in the process of photoreaction from CO₂ to CO [54,55]. Based on the above results, the scheme of electron transport for the BPQDs/CNNT hybrids in catalytic reaction is emerged in Fig. 6e. Under light irradiation, hot electrons excited from BPQDs transmit to CNNT through the interfacial N-P charge transfer channels and ultimately flow to N sites for CO₂ photocatalytic reaction.

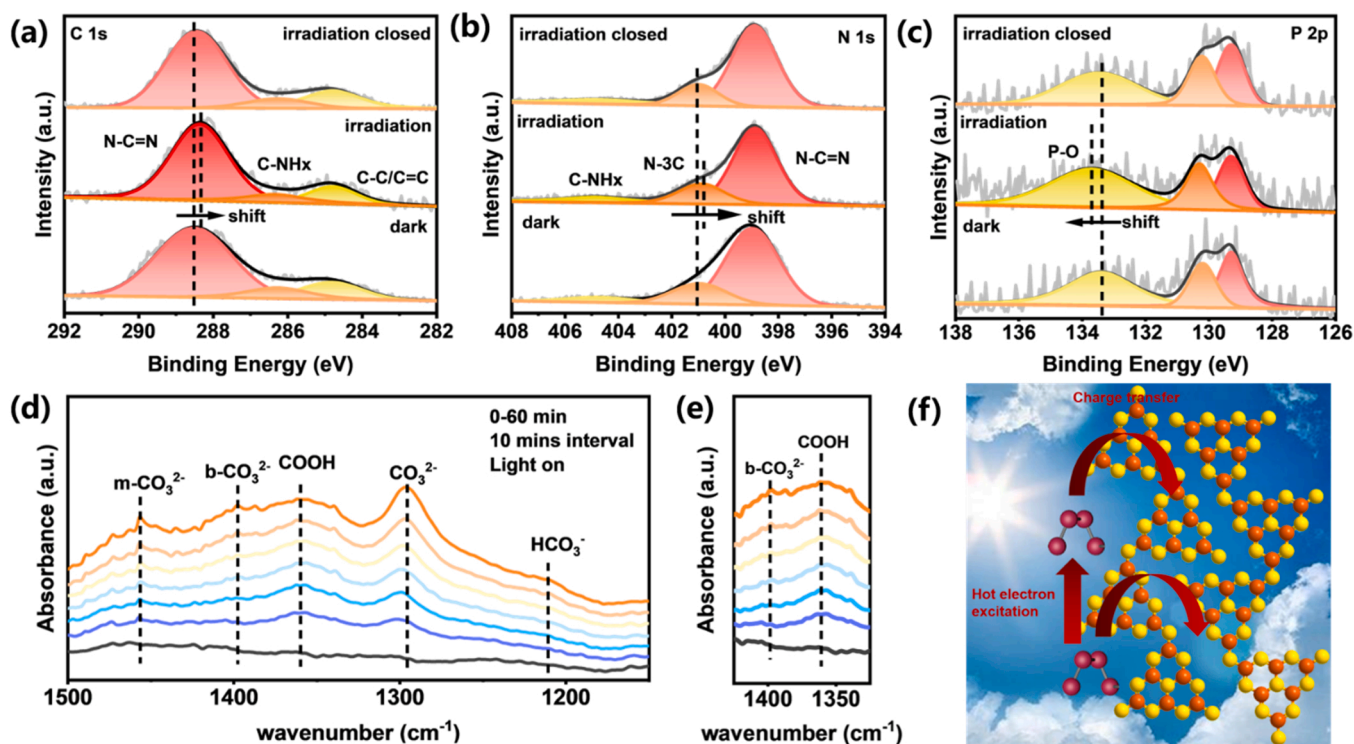


Fig. 6. The in-situ high-resolution XPS spectrum of BPQDs/CNNT: (a) B 1 s, (b) N 1 s and (c) P 2p. (d) in-situ FT-IR spectra of photocatalytic CO₂ reduction process over BPQDs/CNNT hybrid. (e) Enlarged 1325–1425 cm⁻¹ of BPQDs/CNNT (f) scheme of electron transport in catalytic reaction.

4. Conclusion

In summary, we have constructed 0D/1D BPQDs/CNNT hybrid with atomic-level N-P charge transfer channel through an electrostatic assembly method. The modification of BPQDs enhanced the CO₂ photoreduction performance by nearly 3 times that markedly outperforms original CNNT. To explore the reasonable basis underlying the prominent activity, we investigated the precise chemical state between BPQDs and CNNT performing synchrotron radiation XAFS analysis and demonstrated the presence of atomic-level N-P charge transfer channel. The photoinduced charge carriers immigrate from BPQDs to CNNT through the efficient N-P electronic channel as testified by in-situ XPS measurements. This work provides a new sight for the construction of atomic-level charge transfer channel to trigger boosted the separation of electron-hole and the design of BPQDs-anchored heterostructures for enhanced CO₂ photoreduction.

CRediT authorship contribution statement

Zheyang Liu: Data curation, Formal analysis, Investigation, Writing – original draft. **Jianli Liang:** Validation, Formal analysis. **Qianqian Song:** Software. **Yang Li:** Formal analysis. **Zhiqian Zhang:** Formal analysis. **Min Zhou:** Formal analysis. **Wei Wei:** Formal analysis. **Hui Xu:** Supervision. **Chun-Sing Lee:** Writing – review & editing. **Huaming Li:** Resources. **Zhifeng Jiang:** Conceptualization, Formal analysis, Investigation, Methodology, Resources, Supervision, Funding acquisition, Writing – review & editing.

Declaration of Competing Interest

The authors declare that they have no known competing financial interests or personal relationships that could have appeared to influence the work reported in this paper.

Data availability

Data will be made available on request.

Acknowledgement

This work was supported by National Natural Science Foundation of China (Grant No. 22178149, 22178152), Jiangsu Distinguished Professor Program, Natural Science Foundation of Jiangsu Province for Outstanding Youth Scientists (BK20211599), Scientific Research Startup Foundation of Jiangsu University (No. 202096, 22JDG020) and Students Scientific Research Project of Jiangsu University (21A106).

Appendix A. Supporting information

Supplementary data associated with this article can be found in the online version at doi:10.1016/j.apcatb.2023.122472.

References

- [1] D. Wei, R. Sang, P. Sponholz, H. Junge, M. Beller, Reversible hydrogenation of carbon dioxide to formic acid using a Mn-pincer complex in the presence of lysine, *Nat. Energy* 7 (2022) 438–447.
- [2] Y. Wang, X. Shang, J. Shen, Z. Zhang, D. Wang, J. Lin, J.C.S. Wu, X. Fu, X. Wang, C. Li, Direct and indirect Z-scheme heterostructure-coupled photosystem enabling cooperation of CO₂ reduction and H₂O oxidation, *Nat. Commun.* 11 (2020) 3043–3053.
- [3] Z. Jiang, M. Zhou, W. Wei, D. Mao, H. Li, M.K.H. Leung, X. Wang, P.K. Wong, Surface-amino-induced boosting solar conversion of CO₂ to CO over natural metal-free catalyst, *J. CO₂ Util.* 54 (2021), 101773.
- [4] D. Voiry, H.S. Shin, K.P. Loh, M. Chhowalla, Low-dimensional catalysts for hydrogen evolution and CO₂ reduction, *Nat. Rev. Chem.* 2 (2018) 0105.
- [5] A. Weilhard, S.P. Argent, V. Sans, Efficient carbon dioxide hydrogenation to formic acid with buffering ionic liquids, *Nat. Commun.* 12 (2021) 231.
- [6] Q. Yi, W. Li, J. Feng, K. Xie, Carbon cycle in advanced coal chemical engineering, *Chem. Soc. Rev.* 44 (2015) 5409–5445.
- [7] R. Shi, J. Guo, X. Zhang, G.I.N. Waterhouse, Z. Han, Y. Zhao, L. Shang, C. Zhou, L. Jiang, T. Zhang, Efficient wettability-controlled electroreduction of CO₂ to CO at Au/C interfaces, *Nat. Commun.* 11 (2020) 3028.

- [8] Y. Cao, L. Guo, M. Dan, D.E. Doronkin, C. Han, Z. Rao, Y. Liu, J. Meng, Z. Huang, K. Zheng, P. Chen, F. Dong, Y. Zhou, Modulating electron density of vacancy site by single Au atom for effective CO₂ photoreduction, *Nat. Commun.* 12 (2021) 1675.
- [9] X. Shi, Y. Huang, Y. Bo, D. Duan, Z. Wang, J. Cao, G. Zhu, W. Ho, L. Wang, T. Huang, Y. Xiong, Highly selective photocatalytic CO₂ methanation with water vapor on single-atom platinum-decorated defective carbon nitride, *Angew. Chem. Int. Ed.* 61 (2022) e202203063.
- [10] J.W. Fu, J.G. Yu, C.J. Jiang, B. Cheng, g-C₃N₄-based heterostructured photocatalysts, *Adv. Energy Mater.* 8 (2018) 1701530.
- [11] J.L. Liang, Z.F. Jiang, P.K. Wong, C.S. Lee, Recent progress on carbon nitride and its hybrid photocatalysts for CO₂ reduction, *Sol. RRL* 5 (2021) 2000478.
- [12] X. Wang, K. Maeda, A. Thomas, K. Takanabe, G. Xin, J.M. Carlsson, K. Domen, M. Antonietti, A metal-free polymeric photocatalyst for hydrogen production from water under visible light, *Nat. Mater.* 8 (2009) 76–80.
- [13] X.J. Feng, K. Shankar, O.K. Varghese, M. Paulose, T.J. Latempa, C.A. Grimes, Vertically aligned single crystal TiO₂ nanowire arrays grown directly on transparent conducting oxide coated glass: synthesis details and applications, *Nano Lett.* 8 (2008) 3781–3786.
- [14] Y. Li, B. Li, D. Zhang, L. Cheng, Q. Xiang, Crystalline carbon nitride supported copper single atoms for photocatalytic CO₂ reduction with nearly 100% CO selectivity, *ACS Nano* 14 (2020) 10552–10561.
- [15] P. Chen, B. Lei, X. Dong, H. Wang, S. Wang, W. Cui, J. Li, Y. Sun, Z. Wang, F. Dong, Rare-earth single-atom La-N charge-transfer bridge on carbon nitride for highly efficient and selective photocatalytic CO₂ reduction, *ACS Nano* 14 (2020) 15841–15852.
- [16] Y.X. Fang, X.C. Wang, Metal-free boron-containing heterogeneous catalysts, *Angew. Chem. Int. Ed.* 56 (2017) 15506–15518.
- [17] Z.F. Jiang, H.L. Sun, T.Q. Wang, S. Wang, W. Wei, H.M. Li, S.Q. Yuan, T.C. An, H. J. Zhao, J.G. Yu, P.K. Wong, Nature-based catalyst for visible-light-driven photocatalytic CO₂ reduction, *Energy Environ. Sci.* 11 (2018) 2382–2389.
- [18] Z.D. Liu, K.N. Liu, R.C. Sun, J.L. Ma, Biorefinery-assisted ultra-high hydrogen evolution via metal-free black phosphorus sensitized carbon nitride photocatalysis, *Chem. Eng. J.* 446 (2022), 137128.
- [19] Y. Zheng, Z.H. Yu, H.H. Ou, A.M. Asiri, Y.L. Chen, X.C. Wang, Black phosphorus and polymeric carbon nitride heterostructure for photoinduced molecular oxygen activation, *Adv. Funct. Mater.* 28 (2018) 1705407.
- [20] B. Jin, Y. Cho, C. Park, J. Jeong, S. Kim, J. Jin, W. Kim, L. Wang, S. Lu, S. Zhang, S. H. Oh, K. Zhang, J.H. Park, A two-photon tandem black phosphorus quantum dot-sensitized BiVO₄ photoanode for solar water splitting, *Energy Environ. Sci.* 15 (2022) 672–679.
- [21] T. Yin, L. Long, X. Tang, M. Qiu, W. Liang, R. Cao, Q. Zhang, D. Wang, H. Zhang, Advancing applications of black phosphorus and BP-analog materials in photo/electrocatalysis through structure engineering and surface modulation, *Adv. Sci.* 7 (2020) 2001431.
- [22] L.X. Zheng, X.Y. Ye, X.L. Deng, Y.Z. Wang, Y.J. Zhao, X.W. Shi, H.J. Zheng, Black phosphorus quantum dot-sensitized TiO₂ nanotube arrays with enriched oxygen vacancies for efficient photoelectrochemical water splitting, *ACS Sustain. Chem. Eng.* 8 (2020) 15906–15914.
- [23] W. Gao, X.W. Bai, Y.Y. Gao, J.Q. Liu, H.C. He, Y. Yang, Q.T. Han, X.Y. Wang, X. L. Wu, J.L. Wang, F.T. Fan, Y. Zhou, C. Li, Z.G. Zou, Anchoring of black phosphorus quantum dots onto WO₃ nanowires to boost photocatalytic CO₂ conversion into solar fuels, *Chem. Commun.* 56 (2020) 7777–7780.
- [24] L. Kong, Y. Ji, Z. Dang, J. Yan, P. Li, Y. Li, S.F. Liu, g-C₃N₄ loading black phosphorus quantum dot for efficient and stable photocatalytic H₂ generation under visible light, *Adv. Funct. Mater.* 28 (2018) 1800668.
- [25] M.S. Zhu, S. Kim, L. Mao, M. Fujitsuka, J.Y. Zhang, X.C. Wang, T. Majima, Metal-free photocatalyst for H₂ evolution in visible to near-infrared region: black phosphorus/graphitic carbon nitride, *J. Am. Chem. Soc.* 139 (2017) 13234–13242.
- [26] D.Y. He, D.X. Jin, F.Y. Cheng, T.T. Zhang, J. Qu, Y.J. Zhou, X. Yuan, Y.N. Zhang, W. Peijnenburg, Development of a metal-free black phosphorus/graphitic carbon nitride heterostructure for visible-light-driven degradation of indomethacin, *Sci. Total Environ.* 804 (2022), 150062.
- [27] F. Xu, K. Meng, B. Cheng, S. Wang, J. Xu, J. Yu, Unique S-scheme heterojunctions in self-assembled TiO₂/CsPbBr₃ hybrids for CO₂ photoreduction, *Nat. Commun.* 11 (2020) 4613–4621.
- [28] L. Wang, B. Cheng, L. Zhang, J. Yu, In situ irradiated XPS investigation on S-scheme TiO₂/ZnIn₂S₄ photocatalyst for efficient photocatalytic CO₂ reduction, *Small* 17 (2021) 2103447.
- [29] D. Zhao, Y. Wang, C.-L. Dong, Y.-C. Huang, J. Chen, F. Xue, S. Shen, L. Guo, Boron-doped nitrogen-deficient carbon nitride-based Z-scheme heterostructures for photocatalytic overall water splitting, *Nat. Energy* 6 (2021) 388–397.
- [30] H. Ming, P. Zhang, Y. Yang, Y. Zou, C. Yang, Y. Hou, K. Ding, J. Zhang, X. Wang, Tailored poly-heptazine units in carbon nitride for activating peroxymonosulfate to degrade organic contaminants with visible light, *Appl. Catal. B* 311 (2022), 121341.
- [31] W. Lei, Y. Mi, R. Feng, P. Liu, S. Hu, J. Yu, X. Liu, J.A. Rodriguez, J.-o Wang, L. Zheng, K. Tang, S. Zhu, G. Liu, M. Liu, Hybrid OD–2D black phosphorus quantum dots-graphitic carbon nitride nanosheets for efficient hydrogen evolution, *Nano Energy* 50 (2018) 552–561.
- [32] Y. Xu, M. Fan, W. Yang, Y. Xiao, L. Zeng, X. Wu, Q. Xu, C. Su, Q. He, Homogeneous carbon/potassium-incorporation strategy for synthesizing red polymeric carbon nitride capable of near-infrared photocatalytic H₂ production, *Adv. Mater.* 33 (2021), e2101455.
- [33] J. Liang, W. Zhang, Z. Liu, Q. Song, Z. Zhu, Z. Guan, H. Wang, P. Zhang, J. Li, M. Zhou, C. Cao, H. Xu, Y. Lu, X. Meng, L. Song, P.K. Wong, Z. Jiang, C. Lee, *ACS Catal.* 12 (2022) 12217.
- [34] J. Ran, W. Guo, H. Wang, B. Zhu, J. Yu, S.Z. Qiao, Metal-free 2D/2D phosphorene/g-C₃N₄ Van der Waals heterojunction for highly enhanced visible-light photocatalytic H₂ production, *Adv. Mater.* 30 (2018), e1800128.
- [35] X.D. Wang, J. He, J.Y. Li, G. Lu, F. Dong, T. Majima, M.S. Zhu, Immobilizing perovskite CsPbBr₃ nanocrystals on Black phosphorus nanosheets for boosting charge separation and photocatalytic CO₂ reduction, *Appl. Catal. B* 277 (2020), 119230.
- [36] M. Zhu, S. Kim, L. Mao, M. Fujitsuka, J. Zhang, X. Wang, T. Majima, Metal-Free photocatalyst for H₂ evolution in visible to near-infrared region: black phosphorus/graphitic carbon nitride, *J. Am. Chem. Soc.* 139 (2017) 13234–13242.
- [37] B. Wu, L. Zhang, B. Jiang, Q. Li, C. Tian, Y. Xie, W. Li, H. Fu, Ultrathin porous carbon nitride bundles with an adjustable energy band structure toward simultaneous solar photocatalytic water splitting and selective phenylcarbinol oxidation, *Angew. Chem. Int. Ed. Engl.* 60 (2021) 4815–4822.
- [38] K.S. Lakhi, D.-H. Park, G. Singh, S.N. Talapaneni, U. Ravon, K. Al-Bahily, A. Vinu, Energy efficient synthesis of highly ordered mesoporous carbon nitrides with uniform rods and their superior CO₂ adsorption capacity, *J. Mater. Chem. A* 5 (2017) 16220–16230.
- [39] J.H. Lee, J. Ryu, J.Y. Kim, S.-W. Nam, J.H. Han, T.-H. Lim, S. Gautam, K.H. Chae, C.W. Yoon, Carbon dioxide mediated, reversible chemical hydrogen storage using a Pd nanocatalyst supported on mesoporous graphitic carbon nitride, *J. Mater. Chem. A* 2 (2014) 9490–9495.
- [40] X. Zhu, T. Zhang, D. Jiang, H. Duan, Z. Sun, M. Zhang, H. Jin, R. Guan, Y. Liu, M. Chen, H. Ji, P. Du, W. Yan, S. Wei, Y. Lu, S. Yang, Stabilizing black phosphorus nanosheets via edge-selective bonding of sacrificial C60 molecules, *Nat. Commun.* 9 (2018) 4177–4185.
- [41] G. Nicotra, A. Politano, A.M. Mio, I. Deretzi, J. Hu, Z.Q. Mao, J. Wei, A. La Magna, C. Spinella, Absorption edges of black phosphorus: a comparative analysis, *Phys. Status Solidi B* 253 (2016) 2509–2514.
- [42] J. Kruse, P. Leinweber, K.U. Eckhardt, F. Godlinski, Y.F. Hu, L. Zuin, Phosphorus L-2, L-3-edge XANES: overview of reference compounds, *J. Synchrotron Radiat.* 16 (2009) 247–259.
- [43] Y. Li, D. Liu, J. Gan, X. Duan, K. Zang, M. Rønning, L. Song, J. Luo, D. Chen, Sustainable and atomically dispersed iron electrocatalysts derived from nitrogen- and phosphorus-modified woody biomass for efficient oxygen reduction, *Adv. Mater. Interfaces* 6 (2019) 1801623.
- [44] A. Favron, E. Gaufres, F. Fossard, A.L. Phaneuf-L'Heureux, N.Y. Tang, P. L. Levesque, A. Loiseau, R. Leonelli, S. Francoeur, R. Martel, Photooxidation and quantum confinement effects in exfoliated black phosphorus, *Nat. Mater.* 14 (2015) 826–832.
- [45] Y.F. Xu, P.N. Duchesne, L. Wang, A. Tavasoli, A.A. Jelle, M. Xia, J.F. Liao, D. B. Kuang, G.A. Ozin, High-performance light-driven heterogeneous CO₂ catalysis with near-unity selectivity on metal phosphides, *Nat. Commun.* 11 (2020) 5149.
- [46] Q. Liu, H. Cheng, T. Chen, T.W.B. Lo, J. Ma, A. Ling, F. Wang, Boosted CO₂ desorption behaviors induced by spatial dyadic heterostructure in polymeric carbon nitride for efficient photocatalytic CO₂ conversion, *Appl. Catal. B* 295 (2021), 120289.
- [47] J. Zhu, W. Shao, X. Li, X. Jiao, J. Zhu, Y. Sun, Y. Xie, Asymmetric triple-atom sites confined in ternary oxide enabling selective CO₂ photothermal reduction to acetate, *J. Am. Chem. Soc.* 143 (2021) 18233–18241.
- [48] X. Cheng, J. Wang, K. Zhao, Y. Bi, Spatially confined iron single-atom and potassium ion in carbon nitride toward efficient CO₂ reduction, *Appl. Catal. B* 316 (2022), 121643.
- [49] Y. Guo, S. Huang, Y. Guo, Z. Ye, J. Nan, Q. Zhou, Y. Zhu, Efficient degradation of organic pollutants by enhanced interfacial internal electric field induced via various crystallinity carbon nitride homojunction, *Appl. Catal. B* 312 (2022), 121388.
- [50] Y.-J. Yuan, Z.-K. Shen, S. Song, J. Guan, L. Bao, L. Pei, Y. Su, S. Wu, W. Bai, Z.-T. Yu, Z. Ji, Z. Zou, Co-P bonds as atomic-level charge transfer channel to boost photocatalytic H₂ production of Co₂P/black phosphorus nanosheets photocatalyst, *ACS Catal.* 9 (2019) 7801–7807.
- [51] G. Li, Z. Xie, S. Chai, X. Chen, X. Wang, A facile one-step fabrication of holey carbon nitride nanosheets for visible-light-driven hydrogen evolution, *Appl. Catal. B* 283 (2021), 119637.
- [52] L. Liu, H. Zhao, J.M. Andino, Y. Li, Photocatalytic CO₂ reduction with H₂O on TiO₂ nanocrystals: comparison of anatase, rutile, and brookite polymorphs and exploration of surface chemistry, *ACS Catal.* 2 (2012) 1817–1828.
- [53] X. Zu, Y. Zhao, X. Li, R. Chen, W. Shao, Z. Wang, J. Hu, J. Zhu, Y. Pan, Y. Sun, Y. Xie, Ultrastable and efficient visible-light-driven CO₂ reduction triggered by regenerative oxygen-vacancies in Bi₂O₃/CO₃ nanosheets, *Angew. Chem. Int. Ed.* 60 (2021) 13840–13846.
- [54] N.U.A. Frei, Mechanistic study of CO₂ photoreduction in Ti silicalite molecular sieve by FT-IR spectroscopy, *J. Phys. Chem. A* 104 (2000) 7834–7839.
- [55] Z. Jiang, W. Wan, H. Li, S. Yuan, H. Zhao, P.K. Wong, A hierarchical Z-scheme α-Fe₂O₃/C₃N₄ hybrid for enhanced photocatalytic CO₂ reduction, *Adv. Mater.* (2018) 1706108–1706116.